ELSEVIER

Ultramicroscopy 87 (2001) 45–54

ultramicroscopy

www.elsevier.nl/locate/ultramic

Electric charging of thin films measured using the contrast transfer function

Krassimir Danov[1], Radostin Danev, Kuniaki Nagayama*

National Institute for Physiological Sciences, Okazaki National Research Institutes, Myodaiji-cho, Okazaki 444-8585, Japan

Received 13 March 2000; received in revised form 24 July 2000

Abstract

The phase shift of electron waves due to charging of thin films is investigated using the contrast transfer properties of the microscope. We take two photos, one with film at the back focal plane and the other one without film. The phase difference between the contrast transfer functions of the two photos is evaluated using our theoretical predictions. The theoretical model is based on an analytical solution of the Laplace equation with appropriate boundary conditions. From the resulting electrostatic potential function the phase shift of electron waves is derived in a weak lens approximation. With this method, information about the radius of the electron beam and the magnitude of the electrostatic potential at the thin film is obtained. The excellent agreement between the theoretical model and experimental results is observed.

PACS: 61.16.Bg; 41.20.Cv

Keywords: Electric charging; Phase shift; Electrostatic potential; Contrast transfer function

1. Introduction

The charging effect due to electron beam irradiation is a well known and, in most cases, an undesirable effect. The phenomenon has been studied for a long time now but mainly in relation to scanning electron microscopy (SEM) (see the references in Ref. [1]). The conditions in the transmission electron microscope (TEM) are somewhat different in that the specimens are very thin films and the electron energies used are much higher. Detailed description of the process and the resulting macroscopic effects in TEM conditions has been given by Cazeaux [2].

There are few experimental works utilizing electron holography in which the charging of dielectric spheres as well as electric potentials and magnetic fields in solids have been investigated [3–6]. Another application, where electron-induced charging is employed, is the electrostatic phase plate proposed by Unwin [7] which uses the potential produced in the central portion of a thin thread placed on a microscope aperture.

*Corresponding author. Tel.: 81-564-55-7811; fax: 81-564-52-7913.

E-mail address: nagayama@nips.ac.jp (K. Nagayama).

[1] On temporary leave from the Laboratory of Chemical Physics Engineering, Sofia University, 1 J. Bourchier Ave., 1164 Sofia, Bulgaria.

0304-3991/01/$ - see front matter
PII: S0304-3991(00)00061-9

Theoretical modeling of the phase shift of electron waves is based on the numerical solution of the Laplace equation for the electric potential with different geometries of the conducting walls and different boundary conditions [1,8]. Krakow and Siegel [9] investigated, both analytically and experimentally, the transfer characteristics of an electrostatic phase plate similar to one described by Unwin [7] as functions of the magnitude of charge and defocus. Such a model was used in Ref. [10] to describe the electric field induced in insulators by electron bombardment. From the solution of the Laplace equation, Matsumoto and Tonomura [11] proved that the phase shift, which is proportional to the potential integrated along the optical axis, is constant inside the ring of a Boersch-type phase plate. The problem of the determination of the electron wave phase shift becomes more important in thin-film phase plates and thin-foil lens techniques when the charging effect takes place.

In this paper we present a new technique of measuring electron wave phase shift similar to the one proposed by Hoppe (see p. 612 in Ref. [12]). Using the fact that electron waves traveling through an electrostatic field experience a phase shift, our method exploits the influence on the phase contrast transfer properties of the transmission electron microscope. Placing a charged film at the back focal plane of the objective lens results in a change of the phase contrast transfer function. Taking two photos of an amorphous weak-phase object with and without film at the back focal plane, the phase shift by charging is extracted (Section 4.1). In Ref. [12, p. 611] the phase shift measurement in the back focal plane of the objective lens is called "interferometry with the electron microscope". Because in our case the difference between two measurements (photos) is used we will refer to this technique as differential electron interferometry (DEI).

In the electron holography [3–6] the phase shift of the electron waves and the electrostatic potential are measured inside the field of the main electron beam. The DEI measures the potential not only inside the irradiated by the main beam area but also outside where the low-intensity scattered electrons act as a non-influencing probe beam. The sensitivity is very high allowing for measurements of potentials in the order of hundredths of volt. However, some limitations exist: the specimen should be in the form of thin uniform film with constant thickness and isotropic electric properties; the condition investigated is at electrostatic equilibrium and the currents flowing across the film could not be observed.

We propose a theory concerning the spatial dependence of the electrostatic potential. The geometry of the used setup is separated into two parts with different boundary conditions. For each part the Laplace problem for the electrostatic potential function is solved analytically. From the electrostatic potential function the phase shift of electron waves is derived in a weak lens approximation. This theoretical estimation is then used to fit the results from the DEI measurements. In this way, the parameters characterizing the dependence of the electrostatic potential on the surface of the film are calculated.

2. Theory

We will consider the spatial dependence of the electrostatic potential function, $V(r,\ z)$, in the case of axial symmetry, where the radial and vertical coordinates are r and z, respectively (see Fig. 1). The vertical axis of the cylindrical coordinate system coincides with the axis of symmetry and the film is at the plane $z=0$. The film separates the areas of calculations into two parts. We will call the region above the aperture "area I" and the region below the film in the channel of the aperture "area II".

In Ref. [10] in the case of uniform positive charges inside a thin cylinder (polycrystalline or amorphous specimens), the electrostatic potential $V_0(r)$ is given by the relationship (see Eqs. (A.4) and (A.5) in Ref. [10]):

$$V_0(r)=\frac{Q}{4\pi\varepsilon h}\left[1+2\ln\left(\frac{r_0}{a}\right)-\frac{r^2}{a^2}\right]\quad\text{for}\quad 0\leqslant r\leqslant a, \tag{1}$$

$$V_0(r)=\frac{Q}{2\pi\varepsilon h}\ln\left(\frac{r_0}{r}\right)\quad\text{for}\quad a\leqslant r\leqslant r_0. \tag{2}$$

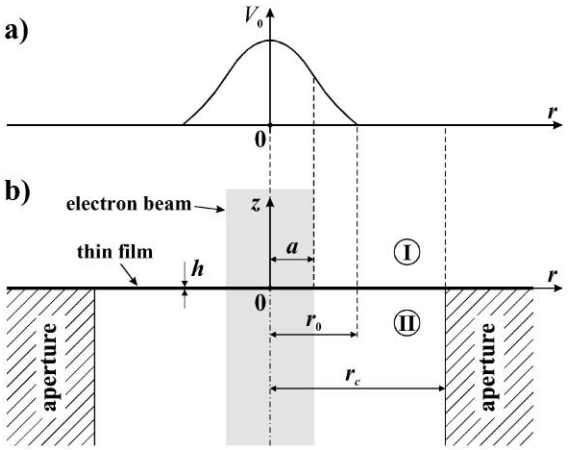

Fig. 1. (a) Electrostatic potential, $V_0(r)$, at the plate. (b) System under consideration: r and z are the coordinates in the cylindrical coordinate system, a is the radius of the electron beam, h is the thickness of the irradiated plate.

where Q is the total charge trapped in the specimen, h is the thickness of the plate, ε is the dielectric constant, a is the radius of the irradiated area, and r_0 is the radius at which the potential becomes zero (see Fig. 1a). Area II is assumed to be an infinite cylinder with radius r_c. At the boundary of area II, $r = r_c$ and $z \leqslant 0$, as well as at the boundary of the area I, $r \geqslant r_0$ and $z = 0$, the potential function V_0 is zero. Generally, r_0 should be equal to r_c, but our experimental results show that $r_0 < r_c$ (see Section 4). From a physical viewpoint the vanishing of the electric potential at the distances $r_0 < r_c$ may be attributed to the following two basic hypotheses:

(i) Secondary electrons coming from the surroundings neutralize the charges on the film. This effect has been observed by Unwin [7] in his electrostatic phase plate experiments.

(ii) The charging occurs mainly at the surface of the film where some contamination could reside. In this case the film is assumed to be conducting and the contamination layer acts as an insulating covering. The second hypothesis seems to be more realistic for our experimental investigations.

In the case of axial symmetry the electrostatic potential function in the working region satisfies the following two-dimensional Laplace equation [1,9,11]:

$$\frac{1}{r}\frac{\partial}{\partial r}\left(r\frac{\partial V}{\partial r}\right) + \frac{\partial^2 V}{\partial z^2} = 0. \tag{3}$$

Solving Eq. (3) with the boundary conditions (1) and (2) gives the electrostatic potential of the whole area and the corresponding phase shift of the electron waves can then be calculated.

2.1. Solution of the Laplace equation for electrostatic potential

In potential theory, the method of separation of variables is used to solve the Laplace equation in cylindrical coordinates. The general solution of Eq. (3) in the finite region II can be expressed in terms of the Fourier–Bessel series (see Eq. (11) in Ref. [1]):

$$V = \frac{Q}{4\pi\varepsilon h}\sum_{k=1}^{\infty} A_k J_0\left(\alpha_k \frac{r}{r_c}\right)\exp\left(\alpha_k \frac{z}{r_c}\right), \tag{4}$$

where J_n is the Bessel function of the nth order. The roots of the zero-order Bessel function, α_k, provide satisfaction of the boundary condition at the aperture wall, $r = r_c$. We chose only the solution with a positive sign in the exponent because of the vanishing of the potential at infinity ($z \to -\infty$). The coefficients A_k, appearing in Eq. (4), are calculated from the boundary condition at the film surface by means of Eqs. (1) and (2). The exact result for them reads (see Appendix A.1) as

$$A_k = \frac{4}{\alpha_k^2 J_1^2(\alpha_k)}\left[\frac{2}{\alpha_k}\frac{r_c}{a} J_1\left(\alpha_k \frac{a}{r_c}\right) - J_0\left(\alpha_k \frac{r_0}{r_c}\right)\right]. \tag{5}$$

In area I above the film, $z \geqslant 0$, the general solution of Eq. (4) can be presented applying the Fourier–Bessel integral transformation as

$$V = \frac{Q}{4\pi\varepsilon h}\int_0^{\infty} \tilde{V}_0(s)\exp\left(-s\frac{z}{r_0}\right) \times J_0\left(s\frac{r}{r_0}\right) s\, \mathrm{d}s, \tag{6}$$

where $\tilde{V}_0(s)$ is the inverse Fourier–Bessel transform of the electrostatic potential function at the film, given by Eqs. (1) and (2). The negative sign in the exponent of solution (6) is used in order to satisfy the boundary condition at infinity ($z \to \infty$).

In Appendix A.2 this image is evaluated and the exact formula for $\tilde{V}_0(s)$ is

$$\tilde{V}_0(s) = \frac{2}{s^2}\left[J_2\left(s\,\frac{a}{r_0}\right) + J_0\left(s\,\frac{a}{r_0}\right) - J_0(s)\right]. \tag{7}$$

For small values of a, r_0, r and z the numerical computation of the integral in Eqs. (6) and (7) is very difficult because of the slow convergence at large values of s. That is why the calculation of the electrostatic potential function is a difficult task. Fortunately, in the experimental work the most important parameter is the radial dependence of the phase shift which is derived in the next section.

2.2. Phase shift of the electron waves

The phase shift of the electron waves, φ, can be estimated in a negligible lens approximation as [14]

$$\varphi = -\pi\,\frac{1+2\alpha U_0}{1+\alpha U_0}\,\frac{1}{\lambda U_0}\left(\int_{-\infty}^{\infty} V\,\mathrm{d}z + hV_0 + hV_{\mathrm{in}}\right), \tag{8}$$

where λ is the electron wavelength, U_0 is the accelerating voltage, $\alpha = 0.9785\times10^{-6}\ \mathrm{V}^{-1}$, and V_{in} is the internal potential which is an intrinsic property of the specimen material. The integral in Eq. (8) represents the influence of the electrostatic potential in the whole working area. It can be divided into two parts:

$$\int_{-\infty}^{\infty} V(r,z)\,\mathrm{d}z = -\frac{Qr_{\mathrm{c}}}{2\pi\varepsilon h}(f_{\mathrm{II}} + f_{\mathrm{I}}), \tag{9}$$

where the dimensionless functions $f_{\mathrm{I}}(r)$ and $f_{\mathrm{II}}(r)$ depend only on the geometry of the electrostatic potential function in areas I and II, respectively.

Knowing the constants A_k from Eq. (5), the exact series for the phase-shift geometrical function, $f_{\mathrm{II}}(r)$, is easy to derive from Eq. (4) as

$$f_{\mathrm{II}} = -\frac{1}{2}\sum_{k=1}^{\infty}\frac{A_k}{\alpha_k}J_0\left(\alpha_k\frac{r}{r_{\mathrm{c}}}\right). \tag{10}$$

In an analogous way, if the dimensionless Fourier–Bessel image $\tilde{V}_0(s)$ is calculated from Eq. (7), then the phase-shift geometrical function $f_{\mathrm{I}}(r)$ is calculated from the following integral:

$$f_{\mathrm{I}} = -\frac{r_0}{2r_{\mathrm{c}}}\int_0^{\infty}\tilde{V}_0(s)J_0\left(s\,\frac{r}{r_0}\right)\mathrm{d}s. \tag{11}$$

For numerical computations series (10) is very convenient but the integral (11) converges very slowly for large values of s. From a physical viewpoint, because of the infinity, the electrostatic potential decreases more slowly in area I than in the area inside the aperture, i.e. $|f_{\mathrm{I}}| > |f_{\mathrm{II}}|$ for each possible value of the radius r. For that reason, we pay special attention to find an analytical result for $f_{\mathrm{I}}(r)$. Using the Weber–Schafheitlin integrals [13] we found the result for $f_{\mathrm{I}}(r)$ in terms of the classical hypergeometric functions, ${}_2F_1$ (see Appendix A.3).

2.3. Numerical results

To show the typical behavior of the electrostatic potential function in the whole working region we calculated the dimensionless potential factor [from Eqs. (4) and (6)]:

$$v(r,z) = \sum_{k=1}^{\infty} A_k J_0\left(\alpha_k\frac{r}{r_{\mathrm{c}}}\right)\exp\left(\alpha_k\frac{z}{r_{\mathrm{c}}}\right) \quad \text{for} \quad r\leqslant r_{\mathrm{c}} \text{ and } z\leqslant 0, \tag{12}$$

$$v(r,z) = \int_0^{\infty}\tilde{V}_0(s)\exp\left(-s\,\frac{z}{r_0}\right)J_0\left(s\,\frac{r}{r_0}\right)s\,\mathrm{d}s \quad \text{for} \quad z\geqslant 0. \tag{13}$$

The geometrical parameters used for calculations depicted in Fig. 2 were the radius of the irradiated area, $a = r_{\mathrm{c}}/6$, and the radius at which the potential becomes zero, $r_0 = r_{\mathrm{c}}/2$. The two-dimensional plot is given in the Cartesian coordinate system, with the center coinciding with the center of the film and x coordinate forward to the aperture. It is well illustrated that the electrostatic potential in area inside the aperture decreases faster than in area I. As expected, at the center of the electron beam the decay length of the electrostatic potential for $z > 0$ is larger than that for $z < 0$. For large distances from the irradiated area the electrostatic potential is different from zero and this fact gives an additional phase shift coming from area I close to the aperture.

In order to demonstrate the influence of the screening of electrostatic potential we calculated the dimensionless phase-shift factors, f_{I} and f_{II}, defined by Eqs. (10) and (11), and the total

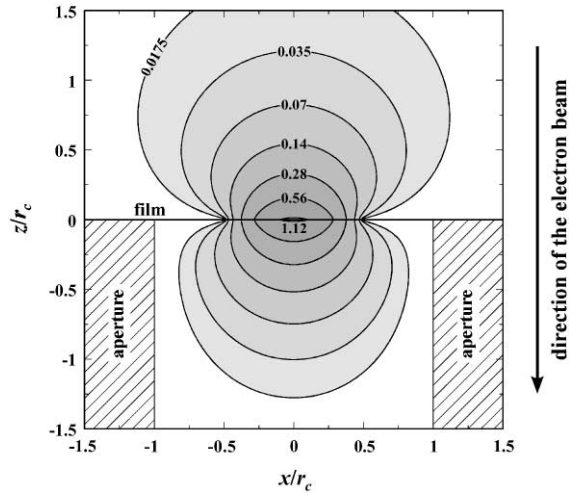

Fig. 2. Typical two-dimensional plot of the dimensionless electrostatic potential function, $v(x, z)$, for $a = r_c/6$ and $r_0 = r_c/2$.

dimensionless phase-shift factor, $f_{tot} \equiv f_I + f_{II}$, for two values of r_0. The numerical results, shown in Figs. 3 and 4, are given for $r_0 = r_c$ and for $r_0 = r_c/3$, respectively. The radius of the irradiated area, a, was kept constant, $a = r_c/6$, in both cases. The general trend of decreasing of the absolute value of the phase shift with distance from the irradiated area is illustrated. Because of the faster decay of the electrostatic potential in the area inside the aperture channel the phase shift factor $|f_{II}|$ is always smaller than the one from the area above the film, $|f_I|$. The difference between them is larger in the case $r_0 = r_c$ (cf. the corresponding curves in Figs. 3 and 4). Moreover, close to the aperture walls the total phase shift is not zero because the electrostatic potential in area I is not zero at $r = r_c$ (see Fig. 2), and therefore it influences the total phase shift through the integral appearing in Eq. (11). The absolute value of the total phase shift at $r = r_c$ in the case $r_0 = r_c/3$ is smaller than that for $r_0 = r_c$. For one and the same total charge trapped in the specimen and radii of the irradiated area, the change of the zeroing distance of the potential at r_0 influences not only the magnitude of the phase shift but also its dependence on the radial distance. The bell-shape behavior of the phase-shift functions becomes more pronounced when $r_0 < r_c$ (see Fig. 4). Comparing

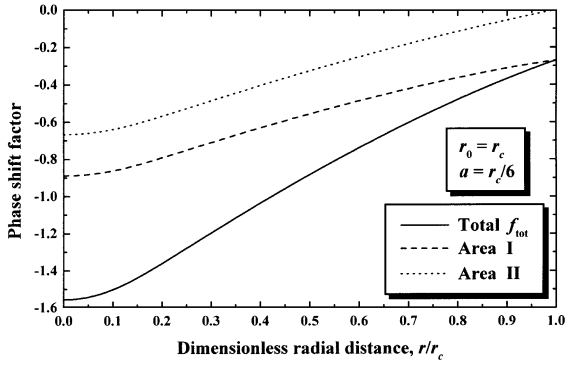

Fig. 3. Radial dependence of the phase-shift factors, f_I, f_{II} and f_{tot}, for $a = r_c/6$ and $r_0 = r_c$.

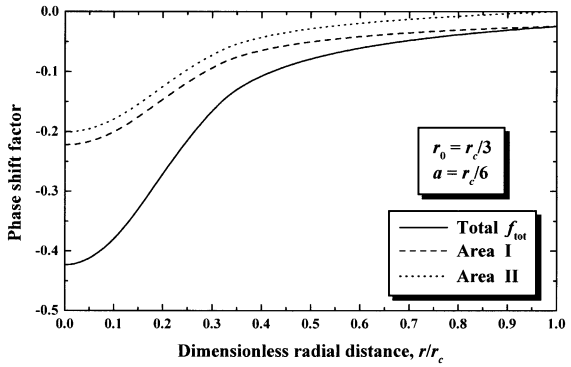

Fig. 4. Phase-shift factors for areas I and II as a function of the radial distance for $a = r_c/6$ and $r_0 = r_c/3$.

the magnitude of dimensionless phase-shift functions depicted in Figs. 3 and 4, we can conclude that the screening of the electrostatic potential suppresses the phase shift about four times.

The total phase shift factor, f_{tot}, is shown for the case $r_0 = r_c$ in Fig. 5, and for the case $r_0 = r_c/3$ in Fig. 6. In both figures the radius of the electron beam, a, was varied from $0.1r_0$ to $0.9r_0$. If the total charge trapped in the specimen is constant while increasing the irradiated area (larger values of a) the resulting electrostatic potential functions are more scattered. Generally, it leads to lower absolute values of the total phase shift. In the case $r_0 = r_c$ (see Fig. 5) the difference between the curves at large radii is more pronounced than for $r_0 = r_c/3$ (Fig. 6), where for large values of r the phase shift comes primarily from the area above the film.

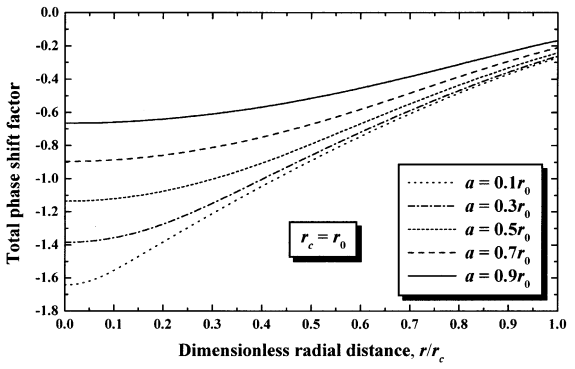

Fig. 5. Total phase-shift factor for $r_0 = r_c$ vs. the radial distance for different radii of the electron beam.

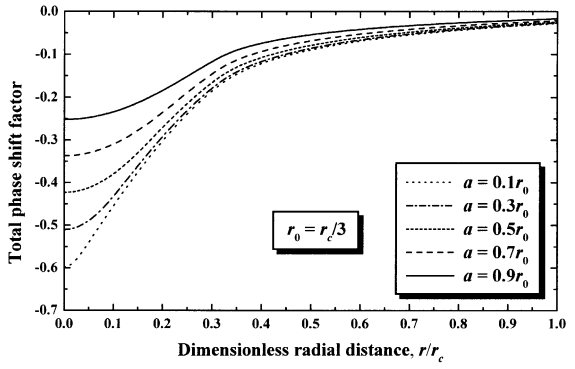

Fig. 6. Total phase-shift factor for $r_0 = r_c/3$ vs. the radial distance for different radii of the electron beam.

3. Experimental procedure

The film being investigated experimentally is placed on a standard objective lens aperture (see Fig. 1b). The aperture is positioned at the back focal plane of the objective lens and centered so that the strong central beam of unscattered electrons passes through the center of the opening. Amorphous carbon film is placed at the specimen plane producing a uniform distribution of scattered electrons. The intensity of the central beam is several orders higher than that of the scattered ones allowing for the assumption that charging takes place mainly in the central area.

In the weak phase object approximation, the phase contrast transfer of the microscope is described by the contrast transfer function $\sin[\gamma(k) + \varphi(k)]$ multiplying the Fourier transform of the object wave. Here $\varphi(k)$ is the phase shift due to charging and $\gamma(k)$ is the one due to defocus and spherical aberration, given by the following relationship [14]:

$$\gamma(k) = 2\pi\left(-\tfrac{1}{2}\lambda\beta k^2 + \tfrac{1}{4}\lambda^3 C_S k^4\right), \tag{14}$$

where λ is the wavelength, β is the defocus, C_S is the spherical aberration coefficient and k is the modulus of the spatial frequency vector. From the Fourier transform of an image it is possible to extract the total phase shift as a function of k by fitting the positions of the extrema in the transfer function. Then, if all the parameters in Eq. (14) are known, $\varphi(k)$ can be evaluated. Spatial frequency k and radial distance r in the back focal plane are related as

$$k = \frac{r}{\lambda f_0}, \tag{15}$$

where f_0 is the focal length of the objective lens. An important requirement is that the phase shift due to charging or due to some varying properties of the film to have axial symmetry.

The DEI has the advantage that it allows for measurement of the potential not only inside the illuminated area but also in the outside area where scattered electrons pass. It is very sensitive allowing for measurement of low surface potentials. On the other hand this could cause problems with rapidly changing or very high potentials in the case of insulating films. The required density of experimental points for the whole range covering the decay of the contrast transfer function (CTF) can be met by combining the data from several photos taken at different defocus β.

4. Experimental results and discussion

4.1. Apparatus and procedure

Amorphous carbon film with thickness around 11 nm was used as a test sample. The film was prepared by vacuum evaporation on freshly cleaved mica, floated on water and transferred on standard 50 μm molybdenum apertures. The experiments were performed by means of a JEOL-4010N transmission electron microscope with

LaB_6 gun operated at 300 kV ($C_S = 3$ mm). At the specimen stage, an amorphous carbon film sample was placed producing a uniform diffraction pattern.

The microscope is aligned and then adjusted at proper magnification and defocus. After inserting the aperture with the film, a photo is taken. The aperture is then changed to one without film and a second photo is taken. From the second photo defocus is measured which is subsequently used to extract only the charging phase shift from the first one. Work in overfocused condition [$\beta < 0$ in Eq. (14)] is preferable since it helps for easier interpretation of the data.

As examples, the CTFs of two images taken at same defocus (−735 nm overfocus) with and without film at the back focal plane are shown in Fig. 7. The CTFs are extracted by means of rotational averaging of the modulus of the Fourier transforms. The corresponding phase shifts due to the aperture foils are shown in Fig. 8.

4.2. Results and discussion

The charging phase shift from two experiments with the same carbon film placed on two apertures was fitted with the proposed theory. The experimental results and the best theoretical fits from Eqs. (10) and (11) are shown in Fig. 9. Very good

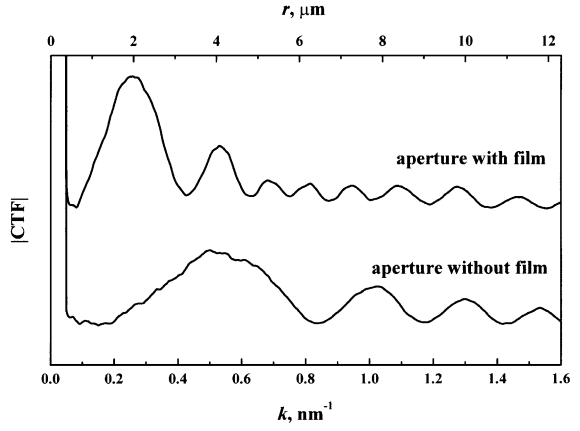

Fig. 7. CTFs of two images taken at same defocus with and without phase shifting film in the back focal plane. The curves are displaced vertically for better viewing.

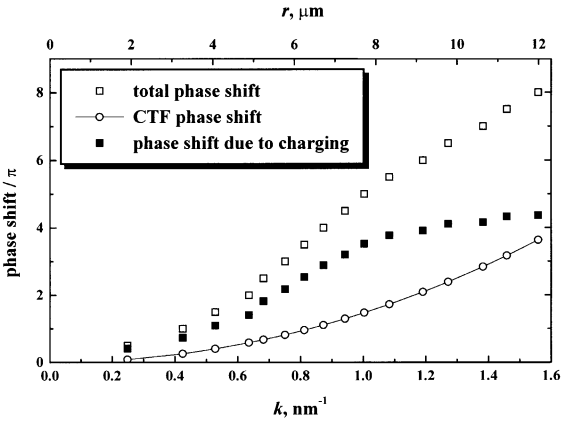

Fig. 8. Illustration of the extraction of the phase shift due to charging. From the total phase shift the one due to CTF is subtracted thus leaving only the phase shift due to charging.

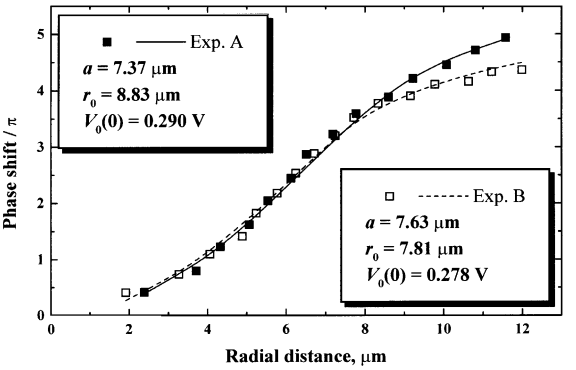

Fig. 9. Experimental results for the phase shifts due to charging (symbols) and best theoretical fits (lines) by the use of Eqs. (10) and (11). The results are from two experiments with the same carbon film placed on two separate apertures.

agreement between the theoretical model and the experimentally measured phase shift is observed. Three parameters are used for the fit, i.e. a, r_0 and V_0. Note that the zero of the phase shift is chosen to be in the center of the film.

Both experiments were performed at approximately identical microscope conditions. The error between the calculated radii of the charged area a is $\pm 1.75\%$ and between the calculated potential in the center of the film $V_0(0)$ is $\pm 2.15\%$. This shows a very good reproducibility. Some differences could arise due to the deviations in the measured

aperture inner diameter. The amorphous carbon is known to be a good conductor making it a preferable choice for specimen support in TEM. The calculated potential of 0.28 V seems to be a reasonable value for conducting films. Surprisingly, the electrostatic potential outside the irradiated area decreases very fast. The radius r_0 at which the potential becomes zero is 1.20 times the radius of the irradiated area a in the first experiment and 1.02 in the second. This fact supports our two hypotheses given in Section 2. The real situation may also be a combination of the above-mentioned effects (i) and (ii). One could also think about many other factors such as: beam-induced heating; beam-induced conductivity; deposit or desorption of matter; surface migration, etc. [15]. All of these make the quantitative description of the situation a more difficult task.

5. Conclusion

The Laplace problem is solved for the case of cylindrical symmetry of the electrostatic potential function. Two sets of boundary conditions are used and for each of them an analytical solution is obtained. The electron wave phase shift is calculated in a weak lens approximation. The experimental results show excellent agreement with the proposed theory. The following conclusions can be drawn:

(i) The investigated amorphous carbon film (thickness 11 nm) is charging positively when irradiated by 300 kV electrons. The fit with the theoretical model gives a value of 0.28 V for the potential in the center of the film. This confirms that the number of emitted secondary electrons is greater than the number of captured incident electrons.

(ii) The phase of the electron wave at the back focal plane is very sensitive to the electrostatic charging of the material film placed there. The phase disturbance of about 5π (see Fig. 9 radial distance from 0 to 12 μm) is caused by electrostatic charging of the film with potential in the center of only 0.28 V. The main part of the phase shift is attributed to the spatial distribution of the electrostatic potential around the film. The theory and experimental procedure described in this paper can be used for the investigation of the charging of thin solid films made from different materials. In this way the best phase-plate material to be used in the complex electron microscopy [16] can be found. The solution of the Laplace equation in the infinite area (Fig. 1b area I) can be readily applied for the calculation of the electrostatic potential distribution around the specimen (in the form of thin film) in the transmission electron microscopy.

Acknowledgements

We are grateful to Dr. K. Murata for helpful discussions and H. Okawara for his help in performing the experiments. One of us (K.D.) is greatly indebted to Monbusho international exchange program for the financial support.

Appendix A

A.1. Calculation of the constants appearing in Eq. (4)

The general solution Eq. (4) has to obey the boundary condition Eqs. (1) and (2) at $z = 0$. Therefore, we have

$$V_0(r) = \frac{Q}{4\pi\varepsilon d}\sum_{k=1}^{\infty} A_k J_0\left(\alpha_k \frac{r}{r_c}\right). \tag{A.1}$$

The Bessel functions in Eq. (A.1) are orthogonal in the interval $[0, r_c]$ and for that reason the constants, A_k, are determined as (see Ref. [13])

$$A_k = \frac{4\pi\varepsilon d}{Q r_c^2}\frac{2}{J_1^2(\alpha_k)}\int_0^{r_0} V_0(r) J_0\left(\alpha_k \frac{r}{r_c}\right) r\,\mathrm{d}r. \tag{A.2}$$

After partial integration of Eq. (A.2) we obtain

$$A_k = -\frac{4\pi\varepsilon d}{Q r_c \alpha_k}\frac{2}{J_1^2(\alpha_k)}\int_0^{r_0} \frac{\mathrm{d}V_0}{\mathrm{d}r} J_1\left(\alpha_k \frac{r}{r_c}\right) r\,\mathrm{d}r. \tag{A.3}$$

If the integral in Eq. (A.3) is separated into two parts, corresponding to the both intervals of the definition for V_0, and Eqs. (1) and (2) are

substituted into Eq. (A.3), the final result reads as

$$A_k = \frac{4}{r_c \alpha_k J_1^2(\alpha_k)} \left[\int_0^a \frac{r^2}{a^2} J_1\left(\alpha_k \frac{r}{r_c}\right) \mathrm{d}r + \int_a^{r_0} J_1\left(\alpha_k \frac{r}{r_c}\right) \mathrm{d}r \right]. \quad (A.4)$$

The two integrals in Eq. (A.4) are table integrals and they can be found in Ref. [13]. Hence the relationship for A_k transforms to

$$A_k = \frac{4}{\alpha_k^2 J_1^2(\alpha_k)} \left[J_2\left(\alpha_k \frac{a}{r_c}\right) + J_0\left(\alpha_k \frac{a}{r_c}\right) - J_0\left(\alpha_k \frac{r_0}{r_c}\right) \right]. \quad (A.5)$$

The simple sum of J_0 and J_2 in Eq. (A.5) reduces it to Eq. (5).

A.2. Calculation of the Fourier–Bessel image appearing in Eq. (6)

If we substitute the boundary condition at $z = 0$ into the general solution Eq. (6), it follows that

$$V_0(r) = \frac{Q}{4\pi\varepsilon d} \int_0^\infty \tilde{V}_0(s) J_0\left(s \frac{r}{r_0}\right) s \, \mathrm{d}s. \quad (A.6)$$

Using the inverse Fourier–Bessel transformation of Eq. (A.6), we derive (see Ref. [13])

$$\tilde{V}_0(s) = \frac{4\pi\varepsilon d}{Q r_0^2} \int_0^\infty V_0(r) \mathrm{J}_0\left(s \frac{r}{r_0}\right) r \, \mathrm{d}r. \quad (A.7)$$

After a partial integration of Eq. (A.7) the integral is simplified to

$$\tilde{V}_0(s) = -\frac{4\pi\varepsilon d}{Q s r_0} \int_0^\infty \frac{\mathrm{d}V_0}{\mathrm{d}r} J_1\left(s \frac{r}{r_0}\right) r \, \mathrm{d}r. \quad (A.8)$$

Following an analogous procedure used in the derivation of Eqs. (A.3) and (A.4), the integral in Eq. (A.8) is separated into two parts and from Eqs. (1) and (2) it can be derived that

$$V_0(s) = \frac{2}{s r_0} \left[\int_0^a \frac{r^2}{a^2} J_1\left(s \frac{r}{r_0}\right) \mathrm{d}r + \int_a^{r_0} J_1\left(s \frac{r}{r_0}\right) \mathrm{d}r \right]. \quad (A.9)$$

The two integrals in Eq. (A.9) are table integrals and they can be found in Ref. [13]. Therefore, the Fourier–Bessel image has the following exact formula:

$$V_0(s) = \frac{2}{s^2} \left[\frac{r^2}{a^2} J_2\left(s \frac{r}{r_0}\right) \Big|_0^a - J_0\left(s \frac{r}{r_0}\right) \Big|_a^{r_0} \right], \quad (A.10)$$

which proves the validity of Eq. (7).

A.3. Calculation of the phase-shift geometrical function, $f_I(r)$

If the formula for the dimensionless Fourier–Bessel image (7) is substituted into the result for the phase-shift geometrical function (11), one can obtain

$$f_I = -\frac{r_0}{r_c} \int_0^\infty \left[J_2\left(s \frac{a}{r_0}\right) + J_0\left(s \frac{a}{r_0}\right) - J_0(s) \right] \times J_0\left(s \frac{r}{r_0}\right) \frac{\mathrm{d}s}{s^2}. \quad (A.11)$$

By using the Weber–Schafheitlin formulas [13] the integral appearing in Eq. (A.11) can be calculated. The result is separated for the following three regions:

(i) in the region of the irradiated area, $0 \leqslant r \leqslant a$:

$$f_I = -\frac{a}{3r_c} F\left(-\frac{3}{2}, \frac{1}{2}; 1; \frac{r^2}{a^2}\right) + \frac{a}{r_c} F\left(-\frac{1}{2}, -\frac{1}{2}; 1; \frac{r^2}{a^2}\right) - \frac{r_0}{r_c} F\left(-\frac{1}{2}, -\frac{1}{2}; 1; \frac{r^2}{r_0^2}\right), \quad (A.12)$$

(ii) in the area $a \leqslant r \leqslant r_0$:

$$f_I = -\frac{a^2}{8 r r_c} F\left(\frac{1}{2}, \frac{1}{2}; 3; \frac{a^2}{r^2}\right) + \frac{r}{r_c} F\left(-\frac{1}{2}, -\frac{1}{2}; 1; \frac{a^2}{r^2}\right) - \frac{r_0}{r_c} F\left(-\frac{1}{2}, -\frac{1}{2}; 1; \frac{r^2}{r_0^2}\right), \quad (A.13)$$

(iii) in the area $r_0 \leqslant r$:

$$f_{\mathrm{I}} = -\frac{a^2}{8rr_{\mathrm{c}}}F\left(\frac{1}{2},\frac{1}{2};3;\frac{a^2}{r^2}\right) + \frac{r}{r_{\mathrm{c}}}F\left(-\frac{1}{2},-\frac{1}{2};1;\frac{a^2}{r^2}\right) - \frac{r}{r_{\mathrm{c}}}F\left(-\frac{1}{2},-\frac{1}{2};1;\frac{r_0^2}{r^2}\right), \tag{A.14}$$

where we denote by F the classical hypergeometric function ${}_2F_1$. The convergence of the series representing the corresponding hypergeometric functions is very fast.

References

[1] E. Plies, in: T. Mulvey, C.J.R. Sheppard (Eds.), Advances in Optical and Electron Microscopy, Vol. 13, Academic Press, New York, 1994, p. 123.

[2] J. Cazaux, Ultramicroscopy 60 (1995) 411.

[3] G. Matteucci, G.-F. Missiroli, E. Nichelatti, A. Migliori, M. Vanzi, G. Pozzi, J. Appl. Phys. 69 (1991) 1835.

[4] B.G. Frost, T.L. Jenkins, J. Microsc. 187 (1997) 85.

[5] B.G. Frost, Ultramicroscopy 75 (1998) 105.

[6] B.G. Frost, E. Voelkl, Ultramicroscopy 72 (1998) 101.

[7] P.N.T. Unwin, Philos. Trans. Roy. Soc. London B 261 (1971) 95.

[8] J. Rouse, in: T. Mulvey, C.J.R. Sheppard (Eds.), Advances in Optical and Electron Microscopy, Vol. 13, Academic Press, New York, 1994, p. 1.

[9] W. Krakow, B. Siegel, Optik 42 (1975) 245.

[10] J. Cazaux, J. Appl. Phys. 59 (1986) 1418.

[11] T. Matsumoto, A. Tonomura, Ultramicroscopy 63 (1996) 5.

[12] F. Thon, in: U. Valdre (Ed.), Electron Microscopy in Material Sciences, Academic Press, London, 1971, p. 571.

[13] M. Abramowitz, I.A. Stegun (Eds.), Handbook of Mathematical Functions with Formulas, Graphs and Mathematical Tables, Applied Mathematics Series, Vol. 55, National Bureau of Standards, New York, 1964.

[14] D. Willasch, Optik 44 (1975) 17.

[15] L. Reimer, Scanning Electron Microscopy, Physics of Image Formation and Microanalysis, Springer, Berlin, 1998.

[16] K. Nagayama, J. Phys. Soc. Japan 68 (1999) 811.